

## ARTICLE

# SERS Platform Based on Diatomite Modified by Gold Nanoparticles Using a Combination of Layer-by-Layer Assembly and Freezing-Induced Loading Method

Received 00th January 20xx,  
Accepted 00th January 20xx

DOI: 10.1039/x0xx00000x

Julijana Cvjetinovic,<sup>\*a</sup> Anastasiia A. Merdalimova,<sup>a</sup> Maria A. Kirsanova,<sup>b</sup> Pavel A. Somov,<sup>b</sup> Daniil V. Nozdriukhin,<sup>a</sup> Alexey I. Salimon,<sup>b</sup> Alexander M. Korsunsky<sup>c</sup> and Dmitry A. Gorin<sup>\*a</sup>

Siliceous diatom frustules represent an up-and-coming platform for a range of bio-assisted nanofabrication processes able to overcome the complexity and high cost of current engineering technology solutions in terms of negligibly small power consumption and environmentally friendly processing combined with unique highly porous structure and properties. Herein, a modification of diatomite – a soft, loose, and fine-grained siliceous sedimentary rock composed of the remains of fossilized diatoms – by gold nanoparticles using layer-by-layer technology in combination with a freezing-induced loading approach is demonstrated. The obtained composite structures are characterized by dynamic light scattering, extinction spectroscopy, scanning (SEM) and transmission electron microscopy (TEM), photoacoustic imaging technique, and tested as a platform for surface-enhanced Raman scattering (SERS) using Rhodamine 6G. SEM, TEM, and energy dispersive X-Ray spectroscopy (EDX), confirmed a dense coating of gold nanoparticles with an average size of 19 nm on the surface of the diatomite and within the pores. The photoacoustic signal excited at a wavelength of 532 nm increases with increasing loading cycles up to three polyelectrolyte-gold nanoparticle bilayers. The hybrid materials based on diatomite modified by gold nanoparticles can be used as SERS substrates, but also as biosensors, catalysts, and platforms for advanced bioimaging.

## Introduction

The fabrication of advanced functional and structural materials using natural materials as templates has become one of the most rapidly growing research areas. One of the novel approaches to the manufacture of composite materials is the use of microorganisms, especially single-celled microalgae, which have an ability to synthesize hierarchically structured composites at the micro- and nanoscale.<sup>1</sup> Diatom algae represent an extremely diverse class of microorganisms, numbering over 100,000 known species<sup>2,3</sup>, with rigid exoskeletons composed of hydrated amorphous silica, called frustules.<sup>4</sup> Such a variety of hierarchically organized highly porous nanostructures combined with the ability to produce hybrid materials with unique physicochemical properties makes them a suitable candidate for different applications in modern science and technology.<sup>3,5–10</sup> Diatoms, as one of the main photosynthesizers, are especially attractive for developing technologies for utilization and storage of carbon dioxide, since they are responsible for producing up to 20% of the oxygen on planet Earth and approximately 40% of marine primary production.<sup>11,12</sup> As a result of photosynthesis, they

produce biomass rich in protein, lipids and other valuable molecules, and at the same time represent a valuable source of nanostructured amorphous silica with huge future potential for various applications.

Diatomite is a light sedimentary rock formed by the accumulation of fossilized remains of unicellular diatom algae on the bottom of oceans and lakes.<sup>13</sup> The main commercial use of processed diatomite is in the food and construction industries, but it also has applications in the chemical, agricultural and related industries.<sup>14–21</sup> Besides, many studies demonstrated the potential of diatomite as a drug delivery system owing to the biocompatibility, non-toxicity, highly porous structure, high surface area, easy functionalization, and low cost.<sup>22–28</sup> The advances made using diatomite as a source of silica, silicon-based materials, and templates for energy-related applications are provided in the latest review article.<sup>29</sup> Through the functionalization of diatomite, its properties and the range of applications can be further upgraded and expanded. Some of the most widely used functionalization approaches include noncovalent and covalent functionalization and chemical conversion of diatomite. The surface of siliceous diatom frustules containing reactive silanol (Si-OH) groups can be readily modified with different functional groups, such as –SH, –NH<sub>2</sub>, –COOH, –CHO for the immobilization of different biomolecular probes (DNA, proteins, antibodies)<sup>30</sup> and drug loading.<sup>23,31–34</sup> The possibility to insert semiconducting or metallic elements, such as germanium<sup>3,35,36</sup>, nickel<sup>37</sup>, titanium<sup>38–40</sup>, aluminum<sup>41</sup>, europium<sup>42</sup>, tin<sup>43</sup>, zirconium<sup>43,44</sup>, in diatom frustules for applications in sensing, optoelectronics, solar energy harvesting, catalysis, and biomedicine is thoroughly explained in the review<sup>45</sup>. Losic and co-workers demonstrated the functionalization of diatomaceous earth with dopamine-modified iron-oxide

<sup>a</sup> Center for Photonic Science and Engineering, Skolkovo Institute of Science and Technology, 3 Nobel Str., Moscow, 121205, Russia.

<sup>b</sup> Center for Energy Science and Technology, Skolkovo Institute of Science and Technology, 3 Nobel Str., Moscow, 121205, Russia.

<sup>c</sup> Department of Engineering Science, University of Oxford, Oxford, OX1 3PJ, United Kingdom.

† Footnotes relating to the title and/or authors should appear here.

Electronic Supplementary Information (ESI) available: [details of any supplementary information available should be included here]. See DOI: 10.1039/x0xx00000x

nanoparticles and proved their capability to be used as magnetically guided micro-carriers for non-invasive and targeted drug delivery.<sup>32</sup> Silver nanoparticles/diatomite nanocomposites exhibited antibacterial effect against infectious pathogens.<sup>46,47</sup>

Among other metallic nanoparticles, gold nanoparticles (AuNPs) gained significant attention and became widely used in the fabrication of new composite materials due to their unique physical and chemical properties, relatively inert nature, robust and highly tunable optical absorption that results from the surface plasmon resonance (SPR) effect.<sup>48</sup> Besides, they are exploited in different fields of biology and medicine such as sensing, targeted drug delivery, imaging, photothermal and photodynamic therapy, as well as the modulation of two or three applications.<sup>49</sup> Jantschke et al. used two approaches—covalent linking and layer-by-layer assembly (LbL)—to decorate diatom frustules with noble metal (Ag, Pt, Au) and semiconductor (CdTe) nanoparticles for surface-enhanced Raman spectroscopy (SERS) of components, for catalysis, and to obtain enhanced image quality in scanning electron microscopy.<sup>50</sup> Fischer and co-workers used a covalent-coupling method to prepare gold nanoparticle-decorated diatom biosilica and successfully applied the obtained catalysts for the oxidation of D-glucose to D-gluconic acid.<sup>51</sup> Pannico et al. used a method based on electroless deposition of gold to cover diatom frustules and showed that such composites could be used as a support for SERS.<sup>52</sup> According to the study by Kong et al., plasmonic nanoparticles decorated diatomite served as a lab-on-a-chip device for on-chip chromatography and label-free biosensing of small molecules from complex biological samples.<sup>53</sup>

Moreover, an ultrasensitive SERS immunoassay based on diatom biosilica with integrated gold nanoparticles has been developed for the detection of interleukin 8 (IL-8) in blood plasma.<sup>54</sup> The results confirmed that diatom frustules increase the sensitivity of the immunosensor when compared with a conventional flat glass-based sensor. It was also demonstrated that diatom shells functionalized with gold nanoparticles via a photo-deposition process could be used for the harvesting and detection of biological analytes, such as bovine serum albumin (BSA), and chemical pollutants (mineral oil) in low dilutions down to  $10^{-16}$  M for BSA and 50 ppm for mineral oil leading to applications in biotechnology, medicine, safety, monitoring and control of environmental hazards.<sup>55,56</sup> Polyethylene glycol (PEG)-modified diatomite decorated with gold nanoparticles by one-pot liquid-phase synthesis demonstrated the potential for usage as advanced nanodevices adding imaging features to the nanocomplexes.<sup>57</sup> Recently, Braceño et al. showed that diatom biosilica modified with gold nanoparticles by In-situ and Ex-situ methods represents a promising candidate for controlled release of the gentamicin in simulated body fluid.<sup>58</sup> The experimental findings showed that while In-situ method resulted in a slower release, the Ex-situ method showed a faster release of gentamicin by using gold/cetyl-trimethylammonium bromide (CTAB) nanoparticles.

In this work, we fabricated gold-coated diatomite composites using for the first time the combination of recently developed freezing-induced loading (FIL) technique<sup>59–62</sup> and LbL assembly.<sup>63–67</sup> These techniques allowed us to obtain different coverage of diatomite by gold nanoparticles, depending on the number of layers. We applied different methods to characterize the prepared composite materials, including dynamic light scattering, extinction spectroscopy, scanning (SEM) and transmission electron microscopy (TEM), energy

dispersive X-Ray analysis (EDX), raster scanning optoacoustic mesoscopy (RSOM), and Raman spectroscopy. Besides, we tested the diatomite functionalized by gold nanoparticles as a SERS platform by using Rhodamine 6G as the probe molecule.

## Experimental

### Materials and methods

**Materials.** A food-grade diatomite powder was obtained from Industrial Company QUANTUM Ltd, (Nikolsk, Russia). Chloroauric acid ( $\text{HAuCl}_4 \times 3\text{H}_2\text{O}$ ), Sodium citrate monobasic ( $\text{HOC}(\text{COONa})(\text{CH}_2\text{COOH})_2$ ), sodium chloride (NaCl), Poly(allylamine hydrochloride) (PAH, Mw = 70 kDa), agarose (low gelling temperature, A-9045), Rhodamine 6G were all purchased from Sigma-Aldrich (Darmstadt, Germany). Deionized (DI) water (specific resistivity higher than 18.2 MΩcm) from a Milli-Q Integral 3 water purification system (Millipore, Burlington, MA, USA), was used to make all solutions.

**Gold nanoparticle synthesis.** Gold nanoparticles were synthesized by standard citrate synthesis. 88 μL of 1 M  $\text{HAuCl}_4$  aqueous solution was diluted to 50 mL by deionized water and heated up to boiling. While boiling, 8.9 mL of 1% sodium citrate tribasic dihydrate was added. The resulting solution (concentration,  $2 \times 10^{12}$  particles/mL) was stirred at boiling temperature for 1 h, then slowly cooled, and stored in the fridge at +4 °C. Gold nanoparticle size and zeta potential were characterized by ZetaSizer Nano ZS analyzer (Malvern Panalytical, Malvern, UK), extinction spectrum was collected by Infinite M Nano+ (Tecan Trading AG, Switzerland).

**Fabrication of gold-coated diatomite.** Before modification, diatomite powder was washed with DI water two times. A standard LbL procedure consists of depositing alternating layers of oppositely charged materials with washing steps in between. Firstly, 20 mg of negatively charged diatomite were suspended in positively charged PAH solution (2 mL; 0.1% PAH in 0.15 M sodium chloride), followed by agitation in a vortex for 15 min. After this standard adsorption procedure, the samples were washed three times with DI by centrifugation using the Centrifuge 5340 (Eppendorf, Germany) (664 × g, 3 min). Gold nanoparticles were subsequently deposited onto the PAH-coated diatomite using FIL approach. Namely, 2 mL of gold nanoparticle solution ( $10^{12}$  particles/mL) were added, and the mixture was placed in a freezer (−20 °C) in a continuously rotating flask for 2 h. After the water was completely frozen, the samples were thawed at room temperature, centrifuged at 664 × g for 3 min, and washed at least three times with DI water, resulting in the formation of a bilayer consisting of a polyelectrolyte/nanoparticle composite. Depending on the sample, the cycle was repeated up to five times to obtain a multilayered composite structure. The resulting composites were stored in water.

**Extinction spectroscopy.** Extinction spectra were recorded with an Infinite M Nano+ (Tecan Trading AG, Switzerland) dual-mode microplate reader at room temperature (25 °C) in the wavelength range 400–700 nm with a 2-nm wavelength step and a 9-nm bandwidth.

**Zeta potential measurements.** Zeta-potential measurements were performed upon deposition of each layer using ZetaSizer Nano ZS analyzer (Malvern Panalytical, Malvern, UK). All samples were diluted 200 times in DI water and placed in the U-cuvette. Measurements were carried out at 25 °C and repeated three times.

**Scanning electron microscopy.** Scanning electron microscopy was performed on a TESCAN SOLARIS S9000 (Brno, Czech Republic) electron microscope in a high vacuum at 5 keV landing energy, 300 pA beam current and with registration of a signal using a backscattered electron detector. Samples were mounted on an aluminum stub using double-sided carbon adhesive tape and were analyzed without applying a conductive coating.

**Transmission electron microscopy and EDX measurements.** Bright field TEM (BF-TEM) images, high angle annular dark-field scanning transmission electron microscopy (HAADF-STEM) images, and energy-dispersive X-ray (EDX) spectra and compositional maps were acquired in a STEM-mode on an aberration-corrected FEI Titan Themis Z (ThermoFisherScientific, Breda, Netherlands) transmission electron microscope equipped with a Super-X detection system and operated at 120 kV. Specimens were prepared by depositing a drop of gold-coated diatomite solution onto a holey copper grid with Carbon/Lacey supporting layer and letting them dry in the air followed by transferring into TEM column.

**Photoacoustic imaging.** The photoacoustic signals from the gold-coated diatomite composites were obtained using RSOM setup Explorer P50 (iTheraMedical GmbH, Germany). For the purpose of imaging, we performed a 2-fold serial dilution of stock suspensions of gold-coated diatomite 5 times. 3  $\mu$ l of these suspensions were mixed with melted agarose gel (7  $\mu$ l), which was previously obtained by dissolving 0.1-g portion of agarose in 10 ml of distilled water at 90 °C. 4- $\mu$ l droplets containing different concentrations of these mixtures were pipetted into a petri dish that was filled with DI water after solidification and placed in the imaging chamber. The samples were illuminated with a Wedge HB frequency-doubled flashlamp-pumped Nd:YAG laser (Bright Solutions, Pavia, Italy) at an excitation wavelength of 532 nm (repetition rate, 1 kHz; pulse energy, 200  $\mu$ J; pulse length, 1 ns). The photoacoustic signal was detected with a custom-made spherically focused LiNbO<sub>3</sub> detector (center frequency, 50 MHz; bandwidth, 11–99 MHz; focal diameter, 3 mm; focal distance, 3 mm). The axial and lateral resolution of the RSOM system is 10  $\mu$ m and 40  $\mu$ m, respectively. The obtained images were processed with ImageJ software. The mean pixel intensity was found from MIP RGB images by analyzing the color histograms of a selected region of interest (ROI), which show the mean pixel intensity for the red (11–33 MHz) and green channels (33–99 MHz).

**SERS measurements.** For SERS measurements, diluted suspensions of gold-coated diatomite consisting of one (Diatomite-(PAH/Au)<sub>1</sub>), three (Diatomite-(PAH/Au)<sub>3</sub>), and five (Diatomite-(PAH/Au)<sub>5</sub>) bilayers were mixed with 0.2 mM Rhodamine 6G in an equal volume and left overnight. The Raman spectra from liquid droplets pipetted onto the quartz glass were collected by a confocal Raman spectrometer (LabRam HR Evolution, HORIBA France SAS, Longjumeau, France) equipped with a 633 nm He-Ne laser excitation source and an Olympus objective (MPlan, 10x). A grating with 600 grooves/mm was used throughout. Spectra were registered in the Raman-shift range

600–1700 cm<sup>-1</sup> at laser power 6.1 mW with a 20 s acquisition time and averaged on 10 accumulations. Baseline correction was provided by instrument-embedded software (LabSpec6, HORIBA France SAS, France) after the signal acquisition.

## Results and discussion

### Gold nanoparticle characterization

Gold nanoparticles can be synthesized using different approaches depending on the desired size, shape, and surface functionality.<sup>68</sup> Here, we used a standard method developed by Turkevich et al.<sup>69</sup> According to bright-field TEM (BF-TEM) image in Figure 1a, the spherical gold nanoparticle sizes follow a normal distribution with an average diameter of 19  $\pm$  5 nm (Figure 1b). The obtained gold nanoparticles have an absorption peak at 524 nm, as shown in Figure 1c. The absorption band results from the collective oscillation of the conduction electrons due to the resonant excitation by the incident photons.<sup>70</sup> Zeta potential measurements showed that the nanoparticles have an average surface charge of  $-29.3 \pm 0.9$  mV, indicating that their stability is on the borderline between incipient instability and moderate stability<sup>71</sup>. Owing to the unique features of gold nanospheres<sup>72</sup>, such as size- and shape-related optoelectronic properties, good biocompatibility, low toxicity, large surface-to-volume ratio, they have been exploited for a wide range of applications in bionanotechnology, diagnostics, imaging, delivery, and therapy.<sup>68,73</sup> However, some of the most important physical properties are surface plasmon resonance, which occurs when free charges on the surface of AuNPs oscillate with the electromagnetic field, and the ability to quench fluorescence.<sup>74</sup> Moreover, AuNPs have been widely used as photoacoustic contrast agents in recent years.<sup>48,75</sup> Considering the abovementioned facts, in this study, we used AuNPs to modify the diatomite surface, expecting excellent photoacoustic and enhanced SERS signals.

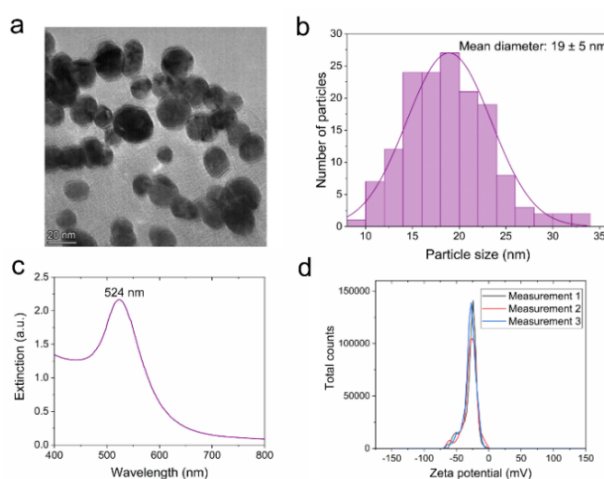


Figure 1 - a) Typical BF-TEM image of gold nanoparticles (scale bar, 20 nm), b) Size distribution histogram of synthesized gold nanoparticles, c) Extinction spectrum of gold nanoparticle, d) Zeta potential distribution of gold nanoparticles.

### Fabrication of gold-coated diatomite

For the deposition of gold nanoparticles onto the surface of diatomite, we applied for the first time the LbL technique in combination with freezing-induced loading. LbL is based on electrostatic interactions between a positively charged polyelectrolyte and, in this case, negatively charged nanoparticles. Therefore, the desired composite material can be obtained by depositing alternating layers of oppositely charged materials with washing steps in between. PAH, as one of the most popular positively charged polyelectrolytes, according to the scheme shown in Figure 2a covers the negatively charged surface of the diatomite and subsequently attracts the negatively charged gold nanoparticles. The LbL+FIL process can be repeated several times, which makes it possible to obtain a high efficiency of nanoparticle deposition. Here, we applied it up to five times, which resulted in hybrid materials based on diatomite with different coverage by gold nanoparticles.

The freezing-induced loading approach is based on the controlled directional freezing, in which the ice crystals grow parallel to the *a*-direction of the hexagonal base and form the so-called cold-finger interfaces.<sup>59</sup> During crystallization, AuNPs and diatomite fragments were pushed by the crystallization front, so the nanoparticles

but after that, we observed the decrease, which may be due to two processes. First, upon each layer deposition, we had to remove the weakly adsorbed polyelectrolytes and nanoparticles by rinsing with deionized water at least three times, which leads to the loss of the certain amount of particles. Therefore, even though the AuNPs can settle on the surface more, due to the smaller number of particles, the absorbance values decrease. According to spectrum of gold-coated diatomite composites consisting of five PAH/AuNPs bilayers, the band at ca. 525 nm practically disappears. On the other hand, we can observe the long tail in the region 560–700 nm, which indicates the presence of aggregates. Thus, the number of small nanoparticles which absorb well at ca. 525 nm decreases, while the number of larger aggregates of various shapes increases.

### Zeta potential measurements

Figure 2c shows the change of zeta potential after each adsorption step depending on the layer number. Even though the AuNPs are negatively charged, upon deposition on PAH-coated diatomite, we did not observe the surface charge change. Usually, repeated

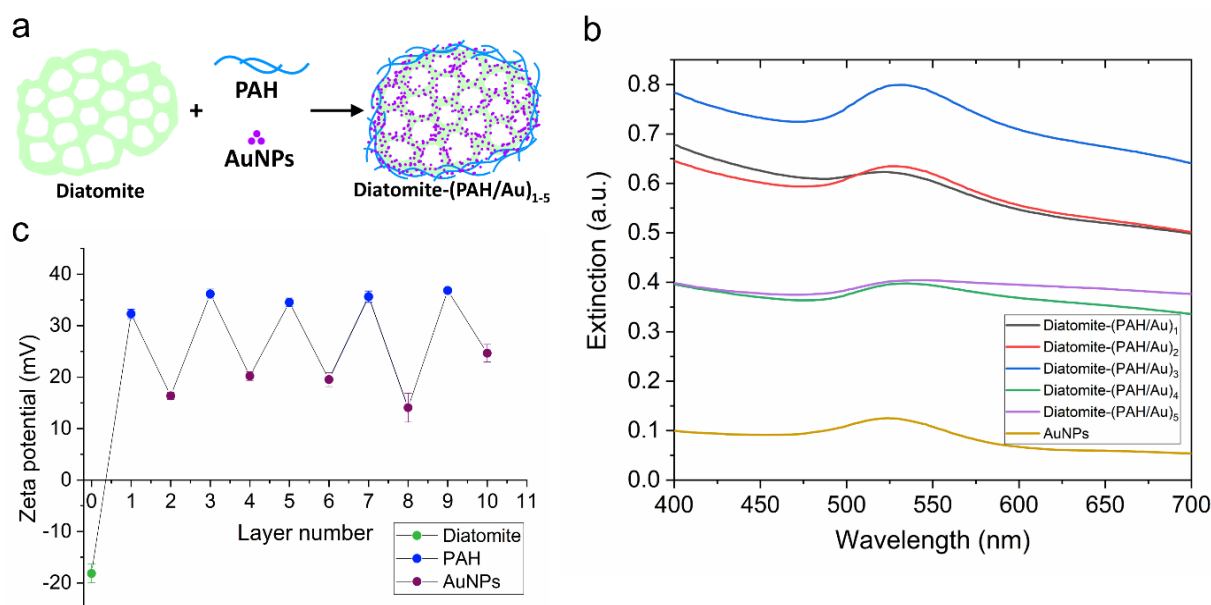


Figure 2 - a) A schematic representation of layer-by-layer approach, b) Extinction spectra of AuNPs and diatomite decorated with different number of PAH/AuNPs bilayers, c) Zeta potential depending on the layer number.

concentrated around the diatomite surface. In the final stage of the process, the nanoparticles were pressed into the surface of the diatomite shards by the growing pressure of the forming ice. German et al. showed that the FIL method leads to a higher amount of magnetite adsorbed into vaterite particles, as compared to the conventional encapsulation methods, such as adsorption and coprecipitation.<sup>59</sup>

### Extinction spectroscopy

Figure 2b shows the extinction spectra of bare AuNPs and gold-coated diatomite hybrid materials consisting of different number of layers. The absorption peak values which correspond to the gold increase with the increasing number of deposition cycles up to three,

adsorption of polyanions and polycations onto the charged particles leads to the change of zeta potential between positive and negative values. However, the absence of negative zeta potential values after depositing AuNPs indicates that they didn't completely cover the surface of diatomite as polyelectrolyte.

### Scanning electron microscopy



SEM images of diatomite decorated with one, three, and five PAH/AuNPs bilayers are shown in Figure 3. We can clearly see the difference in the level of coverage of the diatomite surface by AuNPs.

Overview HAADF-STEM and BF-TEM images of a sample consisting of three PAH/AuNPs bilayers (Diatomite-(PAH/Au)<sub>3</sub>) are shown in Figure 4a-d. In the HAADF-STEM images, the contrast is proportional to squared atomic number, and heavy gold nanoparticles appear as bright spots, while in the BF-TEM the color scheme is different and

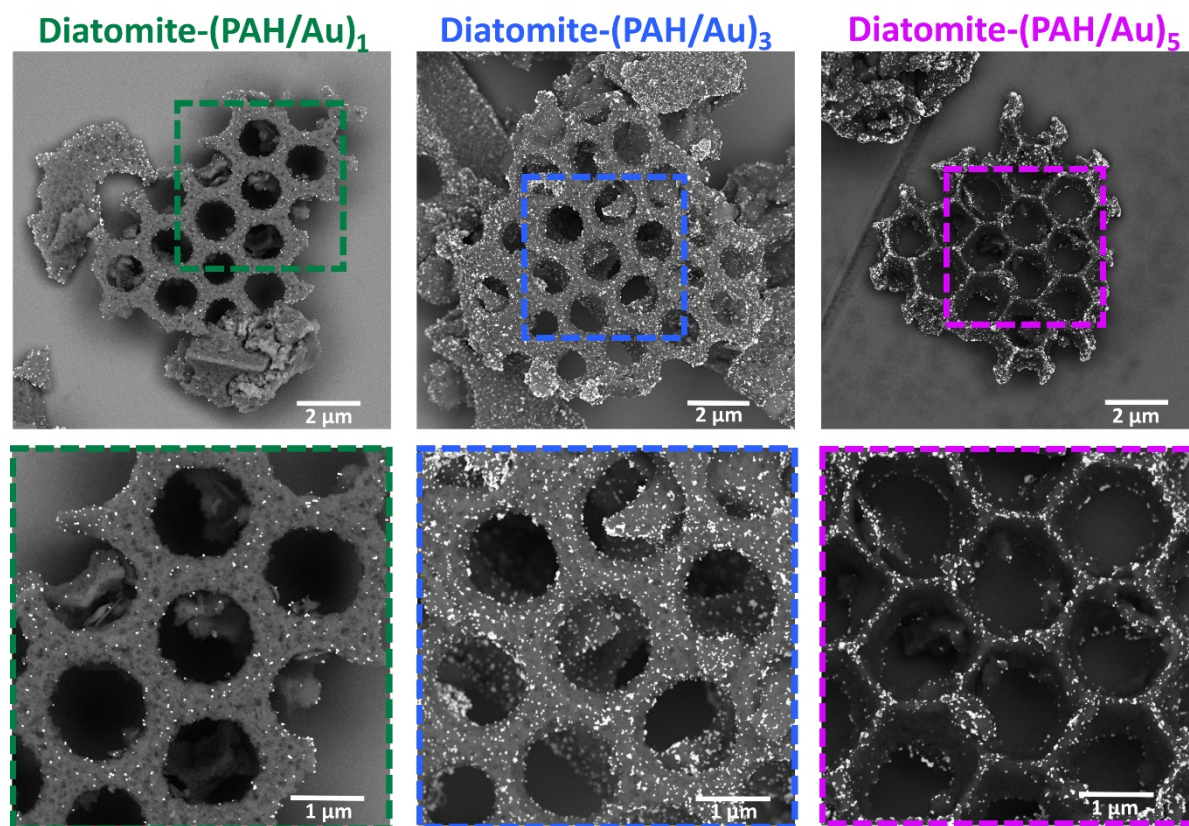


Figure 3 - SEM images of gold-coated diatomite consisting of one (left), three (middle) and five (right) PAH/Au NPs bilayers.

One PAH/AuNPs bilayer leads to insufficient coverage, which significantly increases as the number of bilayers increases. The AuNPs are relatively uniformly distributed onto diatomite templates following their surface morphologies via electrostatic interactions. Nanoparticles are located more at the edges, along the rim, but we can also observe them around the pores. SEM images illustrate that the diatomite surface is not entirely covered with AuNPs, explaining the obtained zeta potential distribution. Usually, nanoparticles at low concentrations are homogeneously adsorbed on the substrates, but at higher concentrations, they tend to form clusters. Some nanoparticles get deposited in the proximity of other particles because, at high concentrations, all the favored sites at the polyelectrolyte surface become immediately occupied.<sup>76,77</sup> Generally, the deposition of a polycation on a surface previously treated and partially covered with negatively charged nanoparticles will occur predominantly on the nanoparticles' surface.<sup>76,78</sup> Subsequently, in the case of multilayer gold deposition, further anionic AuNPs also bind to locations of previously deposited AuNPs, and therefore, clusters are formed.

#### Transmission electron microscopy and STEM-EDX

AuNPs look dark. The diatomite is covered with a dense layer of AuNPs which tend to form clusters, especially along the edges. STEM-EDX maps and spectra confirmed the presence of AuNPs on the surface of diatomite, composed of silica (Figure 4e,f). The dominant peaks in the EDX spectrum arise from oxygen, silicon and gold, as expected. The C and Cu signals are attributed to the supporting TEM grid, though the carbon can be present also due to residual organics in the diatomite powder. The presence of Fe can be explained by the nature of diatomite which is composed of 2.5 wt. % iron oxide; as well, Fe-K can be interpreted as an escape peak of intensive Cu-K $\alpha$  line.

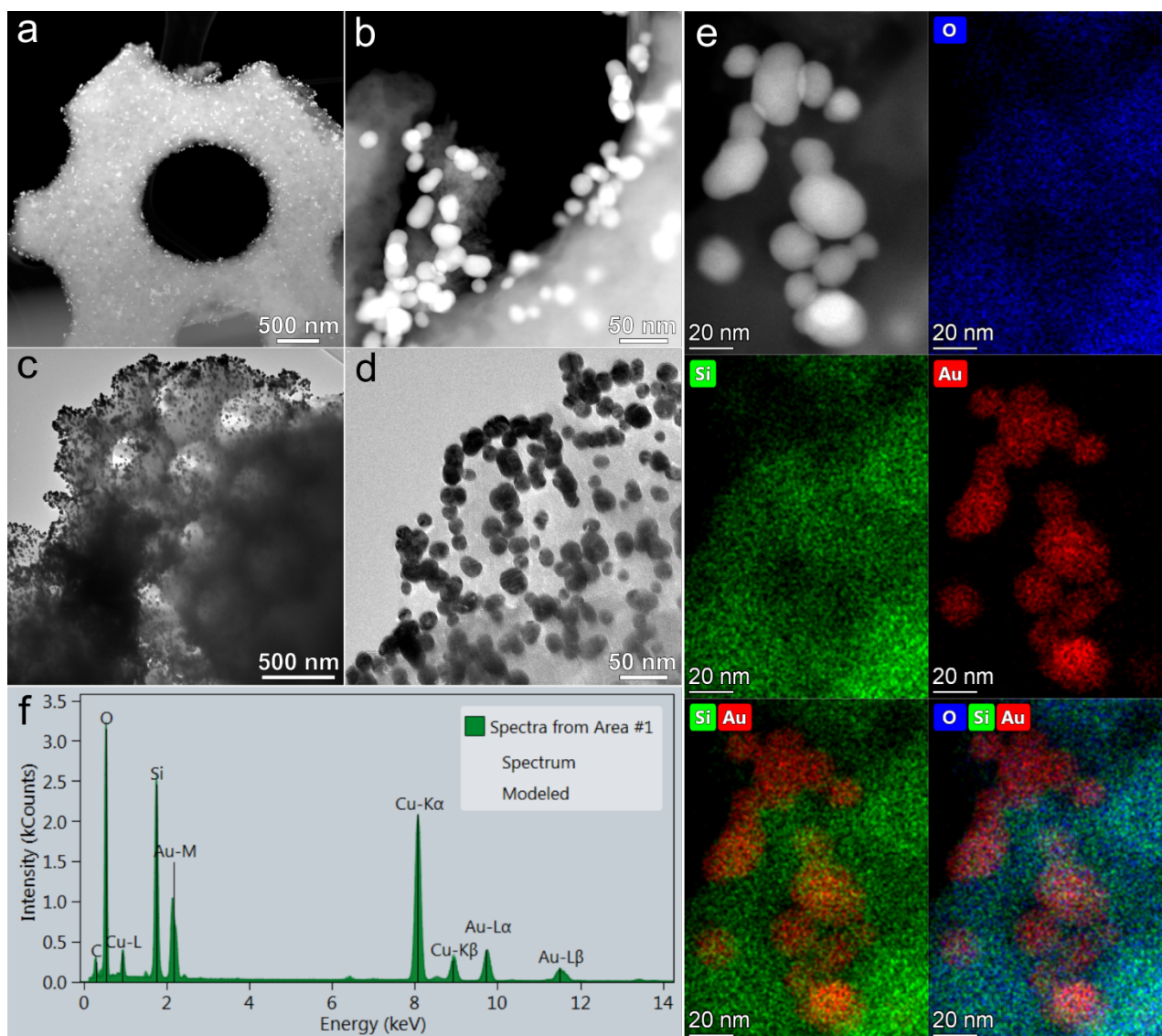


Figure 4 - a,b) HAADF-STEM images of diatomite-(PAH/Au)<sub>3</sub>, c,d) TEM images of diatomite-(PAH/Au)<sub>3</sub>, e) HAADF-STEM image, corresponding elemental EDX maps and f) EDX spectrum of diatomite-(PAH/Au)<sub>3</sub>.

### Photoacoustic imaging

Photoacoustic imaging is based on the photoacoustic effect which implies generation of ultrasound in a material sample upon illumination with nanosecond pulsed laser light via an absorption-based, thermoelastic mechanism.<sup>79</sup> Given the fact that the generated photoacoustic pressure waves are linearly dependent on the absorption coefficient,<sup>80</sup> and thus, proportional to the concentration of gold nanoparticles which absorb well the 532 nm light, it can be used as an *in situ* method for characterizing the degree of modification of diatom biosilica surface with AuNPs. The photoacoustic signals from the gold-coated diatomite composites were collected using RSOM technique. RSOM images of all the fabricated samples are shown in Figure 5. Here we performed a 2-fold dilution to show the dependence of the signal intensity on the

concentration of such hybrid materials. The number of applied PAH/AuNPS bilayers increases from the left to the right side. The images show the signal over the entire frequency range from 11 to 99 MHz. A low-frequency signal in the 11-33 MHz range, emitted by larger particles is shown with red color, while the green-colored high-frequency signal (33-99 MHz) corresponds to smaller objects. The signal decreases with the decrease in concentration, as expected. The red-colored signal is usually higher indicating the aggregation of gold nanoparticles, especially at higher concentrations. On the other hand, the high frequency signal is higher in the case of low number of layers and lower concentrations.

Figure 6a-c illustrates the RSOM signal from the bare AuNPs and stock suspensions of diatomite covered with different number of PAH/AuNPS bilayers in the frequency range 11-99 MHz, 11-33 MHz and 33-99 MHz, respectively. By comparing the collected signals from all samples, we can conclude that the highest value was obtained from the sample with three bilayers (Figure 6d). Here we also compared the extinction at 532 nm and mean pixel intensities in both



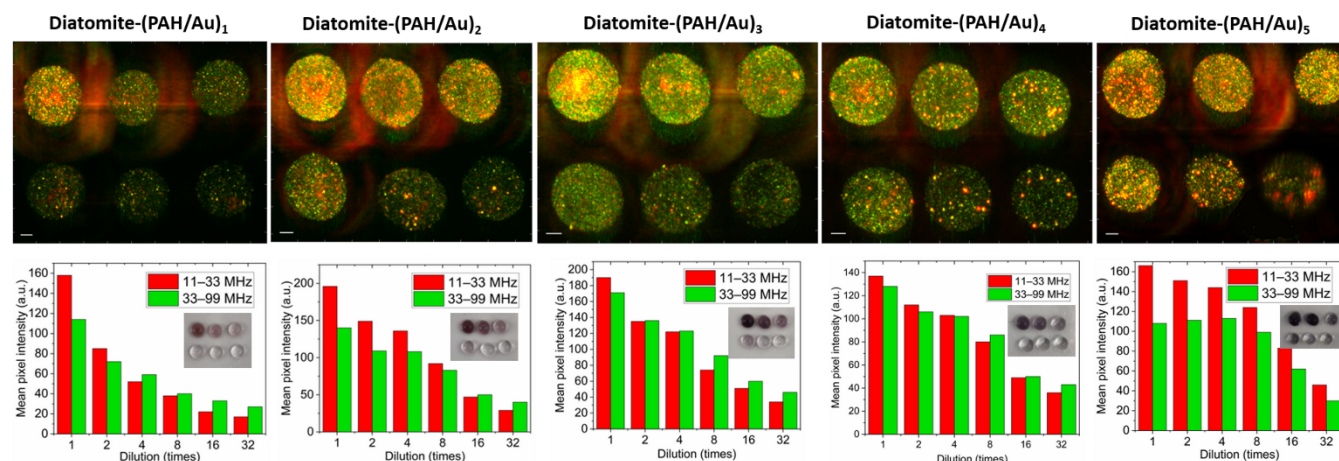


Figure 5 - RSOM images of a 2-fold diluted diatomite coated with different number of PAH/AuNPs bilayers (up) and the corresponding mean pixel intensity vs. dilution (down). Scale bar, 200  $\mu\text{m}$ .

frequency channels (Figure 6e) and observed the good agreement between extinction and signal in the frequency range from 33 to 99 MHz. Low frequency signal deviations can be explained by the tendency of particles to accumulate in the center of the droplet and probably insufficient mixing before measurements.

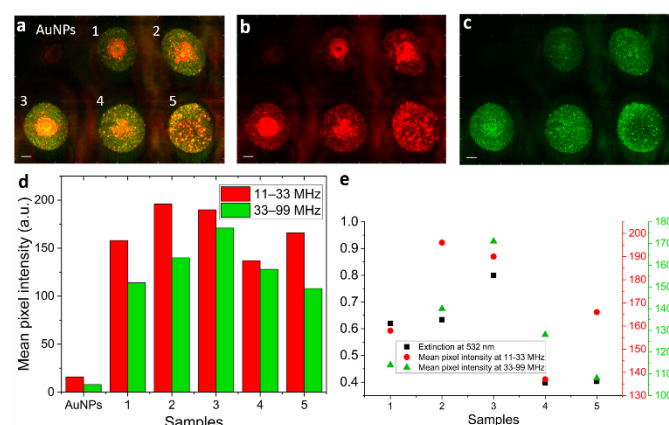


Figure 6 - RSOM images of gold nanoparticles and stock suspensions of diatomite coated with different number of PAH/AuNPs bilayers at: a) 11–99 MHz, b) 11–33 MHz, c) 33–99 MHz frequency range, d) Mean pixel intensity depending on the sample, e) comparison of the extinction at 532 nm and mean pixel intensities at 11–33 and 33–99 MHz. 1-Diatomite-(PAH/Au)<sub>1</sub>, 2-Diatomite-(PAH/Au)<sub>2</sub>, 3-Diatomite-(PAH/Au)<sub>3</sub>, 4-Diatomite-(PAH/Au)<sub>4</sub>, 5-Diatomite-(PAH/Au)<sub>5</sub>. Scale bar, 200  $\mu\text{m}$ .

The signal from the bare AuNPs is very low when compared to that of AuNPs deposited on the diatomite surface. As already mentioned, the gold-based nanoparticles have been widely used as photoacoustic contrast agents owing to their strong and tunable optical absorption that results from SPR effect. When illuminated with a pulsed laser, AuNPs absorb light and generate substantial heat that can sometimes result in their melting. This problem can be solved by silica coating as it lowers the interfacial thermal resistance between gold and the surrounding medium. Moreover, some studies have shown the amplification of photoacoustic signals and the stability generated by silica-coated gold compared to pure gold caused by a decrease in the thermal resistance of gold to the solvent.<sup>81–83</sup>

## SERS measurements

The potential of diatomite embedded with AuNPs to serve as a SERS platform was tested using Rhodamine 6G as a model analyte. The resulting Raman and SERS spectra of droplets containing Rhodamine 6G, bare diatomite and diatomite coated with one, three and five PAH/AuNPs bilayers are shown in Figure 7.

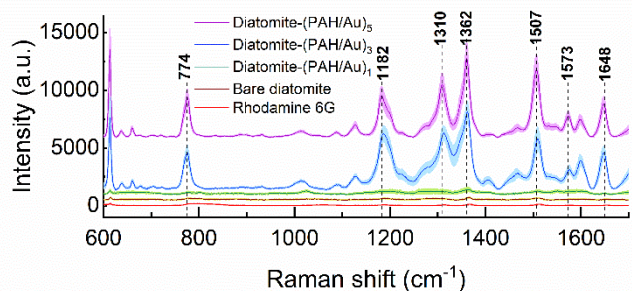


Figure 7 - Surface-enhanced Raman spectra of Rhodamine 6G obtained using gold-coated diatomite hybrid materials with a different number of PAH/AuNPs bilayers.

A variety of strong bands corresponding to Rhodamine 6G on the gold-coated diatomite can be identified in the range between 600 and 1700  $\text{cm}^{-1}$ . Rhodamine 6G provides an intense peak at 613  $\text{cm}^{-1}$ , which is assigned to C–C ring in-plane bending.<sup>84</sup> The vibrational mode of 660  $\text{cm}^{-1}$  band is due to a symmetric deformation localized in the phenyl ring.<sup>85</sup> 774  $\text{cm}^{-1}$  corresponds to the C–H out-of-plane bending vibration, while 1127 and 1182  $\text{cm}^{-1}$  are C–H in-plane bending.<sup>84</sup> Peaks at 1310, 1362, 1507, 1573, 1648  $\text{cm}^{-1}$  are assigned to the aromatic C–C stretching vibrations.<sup>84</sup>

Figure 7 illustrates strong enhancement of SERS signal from Rhodamine 6G using diatomite coated with three and five PAH/AuNPs bilayers compared with bare analyte on the glass slide. A droplet of Rhodamine 6G with Diatomite-(PAH/Au)<sub>3</sub> substrate provided 58 times stronger signal of an analyte, while Diatomite-(PAH/Au)<sub>5</sub> enhanced the signal 53 times, calculated at peak 1368  $\text{cm}^{-1}$  (Table S1, Electronic Supplementary Information (ESI)). On the other hand, the Rhodamine 6G signal when using the substrate containing only one PAH/Au bilayer was not significantly improved. Spectra were collected at ten different points on the surface of the samples, showing a consistent and reproducible scattering pattern

without large variability in the intensity in the case of samples coated with three and five bilayers. A quantitative evaluation of the reproducibility of the spectra in terms of average relative standard deviation (RSD) over the intensities of the prominent Rhodamine 6G Raman peaks are provided in ESI. The enhancement factor (EF) was calculated as follows<sup>86</sup>:

$$EF = \frac{I_{SERS}/N_{surf}}{I_{RS}/N_{vol}} \quad (1)$$

where  $I_{RS}$ ,  $I_{SERS}$  are Raman and SERS intensities of Rhodamine 6G,  $N_{surf}$  is the average number of Rhodamine 6G molecules adsorbed onto the gold-coated diatomite composite in the scattering area for the SERS measurements, and  $N_{vol}$  is the number of Rhodamine 6G molecules present in the bulk scattering volume for spontaneous Raman scattering measurements. For the EF estimation, Raman modes at 1362 and 1509  $\text{cm}^{-1}$  were used, as they correspond to benzene ring stretching and are the most prominent ones. The SERS EF for diatomite coated with three PAH/AuNPs bilayers was calculated to be  $6 \times 10^3$ . Detailed calculation steps are given in ESI. Therefore, hybrid materials based on diatomite decorated with gold nanoparticles can be utilized as a low-cost and easy to fabricate SERS platform.

The signal enhancement introduced by diatomite embedded with gold nanoparticles can be explained from several aspects. Given that diatomite has a high specific surface area, AuNPs can be adsorbed not only on the surface but also around the pores using LbL technique in combination with FIL.<sup>87</sup> Dense gold coating in an ordered manner creates numerous “hot spots” and ensures high SERS enhancement and reproducibility. During multilayer deposition, AuNP clusters are formed, which is indicated by long tail in the extinction spectra of diatomite coated with three and five PAH/AuNPs bilayers (Figure 2b) and confirmed by photoacoustic imaging (Figure 5, 6). Strong SERS enhancement in the case of multilayer deposition, which is absent in the case of one bilayer, is probably resulting from the increase in the number and efficiency of SERS “hot spots” caused by the aggregation of AuNPs with the deposition procedures.

## Conclusions

We report on the successful implementation of a novel approach in the fabrication and characterization of AuNPs-silica sensitive SERS-active materials - LBL+FIL and photoacoustic methods, respectively. LBL+FIL hybrid material fabrication techniques resulted in a strong SERS signal due to the optimization of the spatial distribution of AuNPs over the surface of nanostructured silica substrate. Photoacoustic imaging offers a simple, fast and meaningful technique for the visualization and characterization of obtained materials and many other materials with SERS-active nanoparticles.

## Author Contributions

J.C. – formal analysis, investigation, methodology, visualization, writing – original draft; A.A.M. – formal analysis, investigation, writing – original draft; M.A.K. – formal analysis, investigation, writing – original draft; P.A.S. – formal analysis, investigation; D.V.N. – resources, writing – original draft; A.I.S. –

conceptualization, resources, writing – original draft, writing – review & editing; A.M.K. – conceptualization, supervision, writing – review & editing; D.A.G. – conceptualization, project administration, supervision, validation, writing – review & editing.

## Conflicts of interest

There are no conflicts to declare.

## Acknowledgements

Zeta potential and photoacoustic measurements were performed using the equipment of “Bioimaging and Spectroscopy” Core Facility of the Skolkovo Institute of Science and Technology. “Advanced Imaging” Core Facility of the Skolkovo Institute of Science and Technology is acknowledged for granting access to the TEM facilities.

## Notes and references

- 1 M. Gross, *Curr. Biol.*, 2012, **22**, R581–R585.
- 2 A. Falcatore, M. Jaubert, J. P. Bouly, B. Bailleul and T. Mock, *Plant Cell*, 2020.
- 3 E. De Tommasi, R. Congestri, P. Dardano, A. C. De Luca, S. Managò, I. Rea and M. De Stefano, *Sci. Rep.*, 2018, **8**, 1–14.
- 4 Y. Bedoshvili, K. Gneusheva, M. Popova, A. Morozov and Y. Likhoshvay, *Biol. Open*, 2018, **7**, 1–10.
- 5 A. M. Korsunsky, P. V. Sapozhnikov, J. Everaerts and A. I. Salimon, *Mater. Today*, 2019, **22**, 159–160.
- 6 J. K. Wang and M. Seibert, *Biotechnol. Biofuels*, 2017.
- 7 R. Gordon, D. Losic, M. A. Tiffany, S. S. Nagy and F. A. S. Sterrenburg, *Trends Biotechnol.*, 2009, **27**, 116–127.
- 8 A. Bozarth, U. G. Maier and S. Zauner, *Appl. Microbiol. Biotechnol.*, 2009, **82**, 195–201.
- 9 M. Mishra, A. P. Arukha, T. Bashir, D. Yadav and G. B. K. S. Prasad, *Front. Microbiol.*, 2017.
- 10 N. Nassif and J. Livage, *Chem. Soc. Rev.*, 2011.
- 11 D. M. Nelson, P. Tréguer, M. A. Brzezinski, A. Leynaert and



- B. Quéguiner, *Global Biogeochem. Cycles*, 1995, **9**, 359–372.
- 12 D. L. Rabosky and U. Sorhannus, *Nature*, 2009, **457**, 183–186.
- 13 P. Zahajská, S. Opfergelt, S. C. Fritz, J. Stadmark and D. J. Conley, *Quat. Res. (United States)*, 2020, **96**, 48–52.
- 14 S. É. Ivanov and A. V. Belyakov, *Glas. Ceram. (English Transl. Steklo i Keramika)*, 2008, **65**, 48–51.
- 15 H. E. Galal Mors, *Asian J. Mater. Sci.*, 2010, **2**, 121–136.
- 16 R. Dhanapal, R. Ravindran, N. Seethalakshmi and R. Selvakumar, *J. Radioanal. Nucl. Chem.*, 2019, **319**, 1301–1306.
- 17 S. S. Ibrahim, *J. Int. Environ. Appl. Sci.*, 2012, **7**, 191–199.
- 18 E. L. Aksakal, I. Angin and T. Oztas, *Catena*, 2012, **88**, 1–5.
- 19 M. A. Shah and A. A. Khan, *Int. J. Pest Manag.*, 2014, **60**, 100–113.
- 20 J. Man, W. Gao, S. Yan, G. Liu and H. Hao, *Constr. Build. Mater.*, 2017, **156**, 1035–1042.
- 21 R. B. Owen, R. Potts, A. K. Behrensmeyer and P. Ditchfield, *Palaeogeogr. Palaeoclimatol. Palaeoecol.*, 2008, **269**, 17–37.
- 22 L. De Stefano, I. Rea, N. M. Martucci, P. Arcari, A. Lamberti, I. Ruggiero, R. Tatè, N. Migliaccio, M. Terracciano and I. Rendina, *Nanoscale Res. Lett.*, 2014, **9**, 329.
- 23 I. Ruggiero, M. Terracciano, N. M. Martucci, L. De Stefano, N. Migliaccio, R. Tatè, I. Rendina, P. Arcari, A. Lamberti and I. Rea, *Nanoscale Res. Lett.*, 2014, **9**, 1–7.
- 24 J. Janićijević, D. Krajišnik, B. Čalijsa, V. Dobričić, A. Daković, J. Krstić, M. Marković and J. Milić, *Mater. Sci. Eng. C*, 2014, **42**, 412–420.
- 25 J. Janićijević, D. Krajišnik, B. Čalijsa, B. N. Vasiljević, V. Dobričić, A. Daković, M. D. Antonijević and J. Milić, *Int. J. Pharm.*, , DOI:10.1016/j.ijpharm.2015.10.047.
- 26 J. Janićijević, J. Milić, B. Čalijsa, A. Micov, R. Stepanović-Petrović, M. Tomić, A. Daković, V. Dobričić, B. Nedić
- Vasiljević and D. Krajišnik, *J. Mater. Chem. B*, 2018, **6**, 5812–5822.
- 27 S. Maher, T. Kumeria, M. S. Aw and D. Losic, *Adv. Healthc. Mater.*, 2018, **7**, 1–19.
- 28 I. Rea, N. M. Martucci, L. De Stefano, I. Ruggiero, M. Terracciano, P. Dardano, N. Migliaccio, P. Arcari, R. Tatè, I. Rendina and A. Lamberti, *Biochim. Biophys. Acta - Gen. Subj.*, 2014, **1840**, 3393–3403.
- 29 P. Aggrey, M. Nartey, Y. Kan, J. Cvjetinovic, A. Andrews, A. I. Salimon, K. I. Dragnevski and A. M. Korsunsky, *RSC Adv.*, 2021, **11**, 31884–31922.
- 30 J. Kim, P. Seidler, L. S. Wan and C. Fill, *J. Colloid Interface Sci.*, 2009, **329**, 114–119.
- 31 M. Bariana, M. S. Aw, M. Kurkuri and D. Losic, *Int. J. Pharm.*, 2013, **443**, 230–241.
- 32 D. Losic, Y. Yu, M. S. Aw, S. Simovic, B. Thierry and J. Addai-Mensah, *Chem. Commun.*, 2010, **46**, 6323.
- 33 M. Terracciano, L. De Stefano, H. A. Santos, N. M. Martucci, A. Tino, I. Ruggiero, I. Rendina, N. Migliaccio, C. Tortiglione, A. Lamberti and I. Rea, *Algae - Org. Imminent Biotechnol.*, , DOI:10.5772/63191.
- 34 M. Terracciano, M. A. Shahbazi, A. Correia, I. Rea, A. Lamberti, L. De Stefano and H. A. Santos, *Nanoscale*, 2015, **7**, 20063–20074.
- 35 C. Jeffryes, T. Gutu, J. Jiao and G. L. Rorrer, 2008, **28**, 107–118.
- 36 B. C. Jeffryes, R. Solanki, Y. Rangineni, W. Wang, C. Chang and G. L. Rorrer, 2008, 2633–2637.
- 37 H. E. Townley, K. L. Woon, F. P. Payne, H. White-cooper and A. R. Parker, , DOI:10.1088/0957-4484/18/29/295101.
- 38 C. Jeffryes, T. Gutu, J. Jiao and G. L. Rorrer, 2008, **2**, 2103–2112.
- 39 T. M. W. J. Bandara, M. Furlani, I. Albinsson, A. Wulff and B. E. Mellander, *Nanoscale Adv.*, 2020, **2**, 199–209.
- 40 X. Xiao, X. Zhang, H. Su, S. Chen, Z. He, C. Zhao and S. Yang, *J. Chem.*, , DOI:10.1155/2020/1710989.

## ARTICLE

## Journal Name

- 41 S. Machill, L. Kohler, S. Ueberlein, R. Hedrich, M. Kunasch, S. Paasch, R. Schulze and E. Brunner, *BioMetals*, 2013, **26**, 141–150.
- 42 G. Zhang, W. Jiang, L. Wang, X. Liao, P. Liu, X. Deng and J. Li, *Mater. Lett.*, 2013, **110**, 253–255.
- 43 T. N. Basharina, E. N. Danilovtseva, S. N. Zelinskiy, I. V. Klimenkov, Y. V. Likhoshway and V. V. Annenkov, *Silicon*, 2012, **4**, 239–249.
- 44 K. P. Gannavarapu, V. Ganesh, M. Thakkar, S. Mitra and R. B. Dandamudi, *Sensors Actuators, B Chem.*, 2019, **288**, 611–617.
- 45 W. Brzozowska, M. Sprynskyy, I. Wojtczak, P. Dabek, A. Witkowski and B. Buszewski, *Materials (Basel)*, 2020, **13**, 16–21.
- 46 H. T. Truong, T. D. Nguyen and H. Q. Nguyen, *Aquac. Reports*, 2020, **16**, 100286.
- 47 H. Sun, X. Wen, X. Zhang, D. Wei, H. Yang, C. Li and L. Yang, *J. Nanomater.*, DOI:10.1155/2018/7815810.
- 48 W. Li and X. Chen, *Nanomedicine*, 2015, **10**, 299–320.
- 49 N. Elahi, M. Kamali and M. H. Baghersad, *Talanta*, 2018, **184**, 537–556.
- 50 A. Jantschke, A. K. Herrmann, V. Lesnyak, A. Eychmüller and E. Brunner, *Chem. - An Asian J.*, 2012, **7**, 85–90.
- 51 C. Fischer, M. Adam, A. C. Mueller, E. Sperling, M. Wustmann, K.-H. van Pée, S. Kaskel and E. Brunner, *ACS Omega*, 2016, **1**, 1253–1261.
- 52 M. Pannico, I. Rea, S. Chandrasekaran, P. Musto, N. H. Voelcker and L. De Stefano, *Nanoscale Res. Lett.*, DOI:10.1186/s11671-016-1539-x.
- 53 X. Kong, E. Li, K. Squire, Y. Liu, B. Wu, L. J. Cheng and A. X. Wang, *J. Biophotonics*, 2017, **10**, 1473–1484.
- 54 A. Kamińska, M. Sprynskyy, K. Winkler and T. Szyborski, *Anal. Bioanal. Chem.*, 2017, **409**, 6337–6347.
- 55 V. Onesto, M. Villani, M. L. Coluccio, R. Majewska, A. Alabastri, E. Battista, A. Schirato, D. Calestani, N. Coppedé, M. Cesarelli, F. Amato, E. Di Fabrizio and F. Gentile, *Nanoscale Res. Lett.*, 2018, **13**, 1–9.
- 56 M. Villani, V. Onesto, M. L. Coluccio, I. Valpapuram, R. Majewska, A. Alabastri, E. Battista, A. Schirato, D. Calestani, N. Coppedé, A. Zappettini, F. Amato, E. Di Fabrizio and F. Gentile, *Micro Nano Eng.*, 2019, **2**, 29–34.
- 57 M. Terracciano, M. Napolitano, L. De Stefano, A. C. De Luca and I. Rea, *Nanotechnology*, DOI:10.1088/1361-6528/aab7c4.
- 58 S. Briceño, E. A. Chavez-Chico and G. González, *Mater. Sci. Eng. C*, DOI:10.1016/j.msec.2021.112018.
- 59 S. V. German, M. V. Novoselova, D. N. Bratashov, P. A. Demina, V. S. Atkin, D. V. Voronin, B. N. Khlebtsov, B. V. Parakhonskiy, G. B. Sukhorukov and D. A. Gorin, *Sci. Rep.*, 2018, **8**, 17763.
- 60 M. D. Mokrousov, M. V. Novoselova, J. Nolan, W. Harrington, P. Rudakovskaya, D. N. Bratashov, E. I. Galanzha, J. P. Fuenzalida-Werner, B. P. Yakimov, G. Nazarikov, V. P. Drachev, E. A. Shirshin, V. Ntziachristos, A. C. Stiel, V. P. Zharov and D. A. Gorin, *Biomed. Opt. Express*, 2019, **10**, 4775.
- 61 M. D. Mokrousov, W. Thompson, S. A. Ermilov, T. Abakumova, M. V. Novoselova, O. A. Inozemtseva, T. S. Zatsepin, V. P. Zharov, E. I. Galanzha and D. A. Gorin, *Biomed. Opt. Express*, 2021, **12**, 3181.
- 62 M. V. Novoselova, D. V. Voronin, T. O. Abakumova, P. A. Demina, A. V. Petrov, V. V. Petrov, T. S. Zatsepin, G. B. Sukhorukov and D. A. Gorin, *Colloids Surfaces B Biointerfaces*, 2019, **181**, 680–687.
- 63 G. Decher, *Science (80- )*, 1997, **277**, 1232–1237.
- 64 G. B. Sukhorukov, E. Donath, H. Lichtenfeld, E. Knippel, M. Knippel, A. Budde and H. Möhwald, *Colloids Surfaces A Physicochem. Eng. Asp.*, 1998, **137**, 253–266.
- 65 D. A. Gorin, S. A. Portnov, O. A. Inozemtseva, Z. Lukinska, A. M. Yashchenok, A. M. Pavlov, A. G. Skirtach, H. Möhwald and G. B. Sukhorukov, *Phys. Chem. Chem. Phys.*, 2008, **10**, 6899–6905.
- 66 V. F. Korolovych, O. A. Grishina, O. A. Inozemtseva, A. V. Selifonov, D. N. Bratashov, S. G. Suchkov, L. A. Bulavin, O. E. Glukhova, G. B. Sukhorukov and D. A. Gorin, *Phys. Chem. Chem. Phys.*, 2015, **18**, 2389–2397.
- 67 S. V. German, D. N. Bratashov, N. A. Navolokin, A. A. Kozlova, M. V. Lomova, M. V. Novoselova, E. A. Burilova, V. V. Zhev, B. N. Khlebtsov, A. B. Bucharskaya, G. S. Terentyuk,

- R. R. Amirov, G. N. Maslyakova, G. B. Sukhorukov and D. A. Gorin, *Phys. Chem. Chem. Phys.*, 2016, **18**, 32238–32246.
- 68 Y. C. Yeh, B. Creran and V. M. Rotello, *Nanoscale*, 2012, **4**, 1871–1880.
- 69 J. Turkevich, P. C. Stevenson and J. Hillier, *Discuss. Faraday Soc.*, 1951, **11**, 55–75.
- 70 M. M. Miller and A. A. Lazarides, *J. Opt. A Pure Appl. Opt.*, 2006, **8**, 21556–21565.
- 71 B. Salopek, D. Krasic and S. Filipovic, *Rud. Zb.*, 1992, **4**, 147–151.
- 72 T. K. Sau, A. L. Rogach, F. Jäckel, T. A. Klar and J. Feldmann, *Adv. Mater.*, 2010, **22**, 1805–1825.
- 73 R. X. Xu, *Contrast Media Mol. Imaging*, 2011, **6**, 401–411.
- 74 V. Amendola, R. Pilot, M. Frascioni, O. M. Maragò and M. A. Iatì, *J. Phys. Condens. Matter*, DOI:10.1088/1361-648X/aa60f3.
- 75 R. Cheheltani, R. M. Ezzibdeh, P. Chhour, K. Pulaparthi, J. Kim, M. Jurcova, J. C. Hsu, C. Blundell, H. I. Litt, V. A. Ferrari, H. R. Allcock, C. M. Sehgal and D. P. Cormode, *Biomaterials*, 2016, **102**, 87–97.
- 76 A. M. Yashchenok, D. A. Gorin, M. Badylevich, A. A. Serdobintsev, M. Bedard, Y. G. Fedorenko, G. B. Khomutov, D. O. Grigoriev and H. Möhwald, *Phys. Chem. Chem. Phys.*, 2010, **12**, 10469–10475.
- 77 M. F. Bédard, A. Munoz-Javier, R. Mueller, P. Del Pino, A. Fery, W. J. Parak, A. G. Skirtach and G. B. Sukhorukov, *Soft Matter*, 2009, **5**, 148–155.
- 78 A. M. Yashchenok, O. A. Inozemtseva, D. A. Gorin and B. N. Khlebtsov, *Colloid J.*, 2009, **71**, 422–429.
- 79 R. O. Esenaliev, *J. Biomed. Opt.*, 2017, **22**, 091512.
- 80 R. O. Esenaliev, *Front. Physiol.*, 2017, **8**, 1–6.
- 81 J. V. Jokerst, M. Thangaraj and S. S. Gambhir, in *Photons Plus Ultrasound: Imaging and Sensing 2014*, eds. A. A. Oraevsky and L. V. Wang, SPIE, 2014, vol. 8943, p. 89431O.
- 82 Y. Chen, C. Xu, Y. Cheng and Q. Cheng, *Photoacoustics*, 2021, **23**, 100284.
- 83 Y. S. Chen, W. Frey, S. Kim, P. Kruizinga, K. Homan and S. Emelianov, *Nano Lett.*, 2011, **11**, 348–354.
- 84 X. N. He, Y. Gao, M. Mahjour-Samani, P. N. Black, J. Allen, M. Mitchell, W. Xiong, Y. S. Zhou, L. Jiang and Y. F. Lu, *Nanotechnology*, DOI:10.1088/0957-4484/23/20/205702.
- 85 H. Watanabe, N. Hayazawa, Y. Inouye and S. Kawata, *J. Phys. Chem. B*, 2005, **109**, 5012–5020.
- 86 E. C. Le Ru, E. Blackie, M. Meyer and P. G. Etchegoint, *J. Phys. Chem. C*, 2007, **111**, 13794–13803.
- 87 J. Chen, G. Qin, Q. Chen, J. Yu, S. Li, F. Cao, B. Yang and Y. Ren, *J. Mater. Chem. C*, 2015, **3**, 4933–4944.